



A web of sticky strands: how localized stress controls spatio-temporal fluctuations in viscoelastic flows through a lattice of obstacles

Omar Mokhtari^{1,2}, Michel Quintard¹ and Yohan Davit^{1,†}

¹Institut de Mécanique des Fluides (IMFT), CNRS & Université de Toulouse, 31400 Toulouse, France

²TotalEnergies E&P, CSTJF, 64018 Pau, France

(Received 12 January 2023; revised 31 August 2023; accepted 27 October 2023)

Recent microfluidic experiments have evidenced complex spatio-temporal fluctuations in low-Reynolds-number flows of polymer solutions through lattices of obstacles. However, understanding the nonlinear physics of such systems remains a challenge. Here, we use high performance simulations to study viscoelastic flows through a hexagonal lattice of cylindrical obstacles. We find that structures of localized polymer stress – in particular birefringent strands – control the stability and the dynamics. We first show that, at steady state, strands act as a web of sticky flow barriers that induce channelization, multistability and hysteresis. We then demonstrate that a spontaneous destabilization of the strands drives the transition to unsteady flow with regimes of self-sustained oscillations, travelling waves and strand pulsations. We further show that these pulsations, which result from the destabilization of envelope patterns of stress with strands wrapped around multiple obstacles, are integral to the transition towards elastic turbulence in our two-dimensional simulations. Our study provides a new perspective on the role of birefringent strands and a framework for understanding experimental observations. We anticipate that it is an important step towards unifying existing interpretations of the nonlinear physics of viscoelastic flows through complex structures.

Key words: porous media, viscoelasticity

When a solution of polymers flows past obstacles or through a porous medium, the flexible chains that are transported undergo strong velocity gradients that change their conformation and generate elastic stress (Dauben & Menzie 1967; Seright *et al.* 2011; Kawale *et al.* 2017a; Browne, Shih & Datta 2020b). In turn, this stress modifies the

† Email address for correspondence: yohan.davit@imft.fr

velocity field, leading to a two-way coupling that may induce strong nonlinear effects, such as elastic turbulence (Groisman & Steinberg 2000; Steinberg 2021). Contrary to inertial turbulence, nonlinear viscoelastic effects are predominant for the smallest pores (Poole 2019; Browne *et al.* 2020b), not the largest. Modern experimental approaches have thus exploited microfluidic technologies with pore sizes of several tens to hundreds of micrometres to explore elastic instabilities in complex structures (Kawale *et al.* 2017b).

The most recent microfluidic experiments have used slender cylinders to generate quasi-two-dimensional (quasi-2-D) flows that can be visualized using standard optical microscopy (Haward, Toda-Peters & Shen 2018; Hopkins, Haward & Shen 2020; Haward *et al.* 2021a). This technology has revealed fascinating physics. Spontaneous symmetry breaking and bistability have been shown to occur in the flow of wormlike micellar or hydrolysed polyacrylamide solutions past a single cylinder confined in a channel (Haward *et al.* 2019; Haward, Hopkins & Shen 2020; Hopkins *et al.* 2020). In the case of two cylinders aligned with the flow, a stagnation zone with counter-rotating recirculation vortices appears between the cylinders (Varshney & Steinberg 2017, 2019; Kumar & Ardekani 2021). Flows past two side-by-side cylinders have revealed a series of bifurcations depending on both the gap between cylinders and the Weissenberg number, with symmetric and asymmetric, converging and diverging, bi- and tri-stable states (Hopkins, Haward & Shen 2021; Khan & Sasmal 2021).

Further increasing in complexity, arrays of slender cylinders (Walkama, Waisbord & Guasto 2020; Haward, Hopkins & Shen 2021b) have been used to explore elastic instabilities and transition to chaos in porous structures. Walkama *et al.* (2020) showed that the spatio-temporal velocity fluctuations that develop in a staggered hexagonal lattice of cylinders are suppressed by randomly displacing each cylinder from the crystalline position. They used this observation to argue that disorder suppresses chaos. Haward *et al.* (2021b) showed that introducing disorder into an aligned hexagonal lattice – the set of points that defines the aligned structure being congruent with the staggered one through a rotation of $\pi/6$ modulo $\pi/3$ – yields the opposite effect, with disorder promoting instability. They hypothesized that the important parameter that controls the flow is not disorder, but rather the number of stagnation points accessible to the polymeric chains, with more stagnation points leading to less stability.

Stagnation points induce large molecular strain and represent starting points for the formation of localized regions of large polymer stress known as birefringent strands (Becherer, van Saarloos & Morozov 2009). Strands further induce a feedback on the flow field, essentially acting as a line distribution of forces within an otherwise Newtonian fluid (Harlen, Rallison & Chilcott 1990). We have recently shown in Mokhtari *et al.* (2022) that these structures play a fundamental role in steady viscoelastic flows past obstacles. In arrays of cylinders, they modify the global flow distribution with an increase of stagnation zones and strong channelization. This yields an increase of viscous dissipation in the flow channels and of the rate of entropy generation in the strands. Both these mechanisms generate a surge in resistance to flow through the structure – a phenomenon observed experimentally but not fully understood yet (Galindo-Rosales *et al.* 2012; Clarke *et al.* 2015, 2016; Mitchell *et al.* 2016; Qin *et al.* 2019; Browne & Datta 2021). This evidence that strands are a fundamental component of steady viscoelastic flows past obstacles raises important new questions: What are the feedback mechanisms between flow in these complex geometries, stagnation points on solid obstacle and birefringent strands? Could localized structures of stress, such as strands, be a key to a better understanding of viscoelastic instabilities and chaos in complex structures?

In this article, we use high-performance computing to simulate the flow of viscoelastic fluids through a 2-D hexagonal lattice of obstacles at zero Reynolds number. We solve

A web of sticky strands

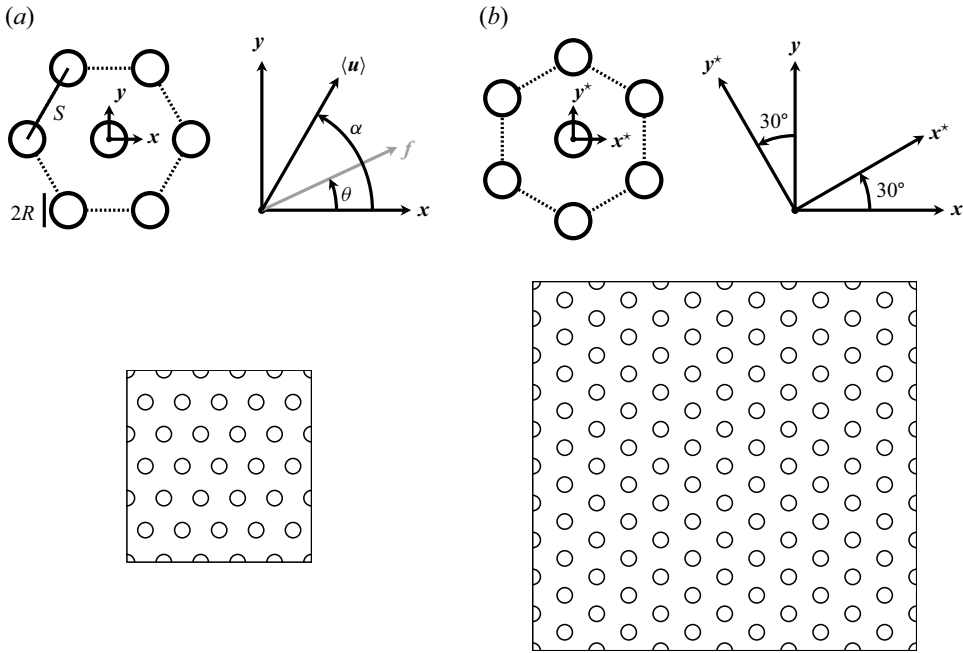


Figure 1. Geometry of the hexagonal lattice of obstacles with aligned and staggered configurations, coordinate systems and angle definitions. (a) Aligned configuration and corresponding coordinate system (x, y) . The radius of each circle is R and the shortest distance between centres of obstacles is S . The unit vector \mathbf{f} is the force density in the non-dimensionalized momentum transport equation and forms an angle θ with x . Here, $\langle \mathbf{u} \rangle$ is the intrinsic average of the velocity field $\langle \mathbf{u} \rangle = 1/|\Omega| \int_{\Omega} \mathbf{u} \, d\Omega$ and forms an angle α with x . (b) Staggered configuration and corresponding coordinate system (x^*, y^*) . The staggered periodic pattern can be obtained by rotating the aligned one by an angle of 30° .

incompressible Oldroyd-B, FENE-CR (Finite Extendable Non-linear Elastic – Chilcott and Rallison) and FENE-P (Finite Extendable Non-linear Elastic – Peterlin) models with an imposed force density in the momentum transport equation and biperiodic boundary conditions. By varying the orientation of the forcing term, the Weissenberg number Wi and the ratio of viscosities β , we explore the physics of viscoelastic flows in a variety of configurations, including both the aligned and staggered cases.

1. Methods

1.1. Domain and boundary conditions

We consider a simulation domain that is a rectangle with biperiodic left/right and top/bottom conditions and a no-slip/no-penetration condition on the boundaries of the obstacles. We have two geometries with a hexagonal lattice of cylindrical obstacles (figure 1). The first one, which is used for studying multistability and steady flow, consists of 30 cylinders in the aligned configuration. The second one, which is used for unsteady flow, is larger and consists of 120 cylinders in the staggered configuration.

1.2. Flow equations

We consider an incompressible flow with $\text{div } \mathbf{u} = 0$ and steady momentum transport given by

$$0 = -\nabla \mathbf{p} + \text{div} (\boldsymbol{\tau}_s + \boldsymbol{\tau}_p) + \mathfrak{F}, \quad (1.1)$$

with \mathbf{u} the velocity, p the pressure, τ_s the solvent stress tensor, τ_p the polymer stress tensor and \mathfrak{F} the imposed force density. This choice of imposing a pressure gradient through \mathfrak{F} , rather than through the boundary conditions, is natural when working with periodic boundary conditions and eliminates boundary effects or instabilities specific to Dirichlet and Neumann conditions – the idea is that of an ‘infinite’ porous medium.

The constitutive stress relation for the solvent is

$$\tau_s = \eta_s (\nabla \mathbf{u} + (\nabla \mathbf{u})^\top) \quad (1.2)$$

with η_s the viscosity. The general form of the polymer stress tensor is

$$\tau_p = \frac{\eta_p}{\lambda} (g(\mathbf{c}) \mathbf{c} - h(\mathbf{c}) \mathbf{I}_d) \quad (1.3)$$

with η_p the polymer viscosity, λ a characteristic time for polymer relaxation and \mathbf{c} the conformation tensor. We consider the Oldroyd-B, FENE-CR and FENE-P models with

$$g(\mathbf{c}) = h(\mathbf{c}) = 1, \quad (1.4)$$

for the Oldroyd-B,

$$g(\mathbf{c}) = h(\mathbf{c}) = \frac{b}{b - \text{tr}(\mathbf{c})}, \quad (1.5)$$

for the FENE-CR and

$$g(\mathbf{c}) = \frac{b}{b - \text{tr}(\mathbf{c})}, \quad h(\mathbf{c}) = \frac{b}{b - \text{tr}(\mathbf{I}_d)}, \quad (1.6a,b)$$

for the FENE-P. In both FENE models, b is the parameter that controls the maximum stretching of the polymers with $\text{tr}(\mathbf{c}) < b$. The Oldroyd-B model is based upon an affine relation between τ_p and \mathbf{c} , which can be interpreted as a Hookean entropic spring description in a molecular dumbbell representation (Bird *et al.* 1987). This model imposes no limit upon the stretching of the molecules and can lead to stress singularity (Shaqfeh & Khomami 2021). FENE-type models limit the trace of the conformation tensor, thus limiting the maximum stretching of the chains (Bird *et al.* 1987). FENE-CR and FENE-P models differ in their response to shear flow: the FENE-CR model represents a Boger fluid, whereas the FENE-P model is shear thinning (Herrchen & Öttinger 1997).

The last constitutive equation is the transport of the conformation tensor, which reads

$$\partial_t \mathbf{c} + (\mathbf{u} \cdot \nabla) \mathbf{c} = \nabla \mathbf{u} \mathbf{c} + \mathbf{c} (\nabla \mathbf{u})^\top - \frac{1}{\eta_p} \tau_p. \quad (1.7)$$

1.3. Non-dimensionalization

To non-dimensionalize the problem, we use the minimum distance between two obstacles, $H = S - 2R$, as a characteristic length. We also use the expression

$$U = \frac{H^2}{\eta_s + \eta_p} \|\mathfrak{F}\|, \quad (1.8)$$

for the reference velocity and H/U as a characteristic time. This reference velocity can be understood as an estimation of the Darcy velocity in the Newtonian case, with H^2 an estimate of the permeability, $\eta_s + \eta_p$ the viscosity and $\|\mathfrak{F}\|$ a norm of the pressure gradient.

The final dimensionless equations read

$$0 = -\nabla p + \nabla^2 \mathbf{u} + \frac{\beta}{Wi} \operatorname{div} (g(\mathbf{c}) \mathbf{c} - h(\mathbf{c}) \mathbf{I}_d) + (1 + \beta) \mathbf{f}, \quad (1.9)$$

$$0 = \operatorname{div} \mathbf{u}, \quad (1.10)$$

$$\partial_t \mathbf{c} + (\mathbf{u} \cdot \nabla) \mathbf{c} = \nabla \mathbf{u} \mathbf{c} + \mathbf{c} (\nabla \mathbf{u})^\top - \frac{1}{Wi} (g(\mathbf{c}) \mathbf{c} - h(\mathbf{c}) \mathbf{I}_d), \quad (1.11)$$

with the viscosity ratio defined as

$$\beta = \frac{\eta_p}{\eta_s}, \quad (1.12)$$

the Weissenberg number as

$$Wi = \frac{\lambda H}{\eta_s + \eta_p} \|\mathfrak{F}\|, \quad (1.13)$$

and the pressure, velocity and force density as

$$p = \frac{1 + \beta}{\|\mathfrak{F}\|} \mathfrak{p}, \quad \mathbf{u} = \frac{\mathbf{u}}{U}, \quad \mathbf{f} = \frac{\mathfrak{F}}{\|\mathfrak{F}\|}. \quad (1.14a-c)$$

It is important to note that, with this definition of the reference velocity, the Weissenberg number Wi does not depend on the actual average flow velocity, but rather on the volume source term $\|\mathfrak{F}\|$. This is a natural choice in our setting since flow results from this volume source term and not from an imposed flow on the boundary conditions. Working with the average flow velocity is possible but unpractical as it is not known *a priori* but rather results from each simulation. One caveat of our definition in (1.13) is that comparison with transition values of Wi from works using the more standard definition is not straightforward – keeping in mind that no comparison with experiments is ever straightforward as viscoelastic models are widely accepted as not being accurate in estimating these transition values. Our largest Wi values, for example, would be much smaller with a definition based on the average flow velocity. For comparison with other works, we provide in the supplementary material available at <https://doi.org/10.1017/jfm.2023.916> the equivalent numbers for a more classical definition of the Weissenberg number.

1.4. Numerical scheme and implementation

A detailed presentation of the numerical scheme is available in Mokhtari *et al.* (2023). Momentum transport is solved via a staggered grid scheme using the Rannacher and Turek low-order finite elements (Rannacher & Turek 1992). The discrete conformation tensor unknowns are located at the centres of the cells and the corresponding transport equation (1.11) is solved using a finite-volume scheme.

The mesh is structured and uniform. It consists of quadrilateral cells with obstacles obtained by making holes into the uniform mesh and circle boundaries approximated as stair steps (see Mokhtari *et al.* (2022) and more details in the supplementary material). In studying the transition to unsteady flows in the staggered case, we took care of working with structured meshes that were symmetric about the horizontal configuration of the strands corresponding to base flow at steady state. We used a constant mesh size $\simeq 0.04R$, where R is the circle radius. This corresponds to approximately 3×10^5 cells and approximately 1.2 million cells for the two geometries presented in figure 1.

At time $t = 0$, the velocity, pressure and conformation fields are initialized as $\mathbf{u} = (0, 0)^\top$, $p = 0$ and $\mathbf{c} = \mathbf{I}_d$. The time discretization consists of a fractional step approach

where (1.9) and (1.10) are decoupled from (1.11) using a beginning-of-step approximation of the latter. Given \mathbf{c}^n , the value of the conformation tensor at time iteration n , we calculate the pressure and velocity at time iteration $n + 1$ by solving

$$0 = -\nabla p^{n+1} + \nabla^2 \mathbf{u}^{n+1} + \mathbf{S}^n, \tag{1.15}$$

$$0 = \operatorname{div} \mathbf{u}^{n+1}, \tag{1.16}$$

with $\mathbf{S}^n = (\beta/Wi)\operatorname{div}(g(\mathbf{c}^n)\mathbf{c}^n - h(\mathbf{c}^n)\mathbf{I}_d) + (1 + \beta)\mathbf{f}$ the source term. For each time step, this Stokes problem is solved in an iterative way through a standard projection scheme that decouples the momentum balance equation from the divergence constraint. For each sub-iteration $k + 1$, the method makes an initial prediction $\tilde{\mathbf{u}}_{k+1}$ of the velocity using the pressure gradient ∇p_k , starting from $\mathbf{u}_0 = \mathbf{u}^n$ and $p_0 = p^n$. The correction step then consists in determining p_{k+1} and correcting \mathbf{u}_{k+1} in such a way that the incompressibility condition (1.16) is respected. This prediction–correction scheme reads

$$\left. \begin{aligned} & \text{Prediction step – Solve for } \tilde{\mathbf{u}}_{k+1} : \\ & \xi (\tilde{\mathbf{u}}_{k+1} - \mathbf{u}_k) + \nabla p_k - \nabla^2 \tilde{\mathbf{u}}_{k+1} + \mathbf{S}^n = 0. \\ & \text{Correction step – Solve for } p_{k+1} \text{ and } \mathbf{u}_{k+1} : \\ & \xi (\mathbf{u}_{k+1} - \tilde{\mathbf{u}}_{k+1}) + \nabla (p_{k+1} - p_k) = 0, \\ & \operatorname{div} \mathbf{u}_{k+1} = 0, \end{aligned} \right\} \tag{1.17}$$

where $\xi > 0$ is a constant that can be understood as the inverse of a time step. Convergence is considered to be reached when the relative difference between two consecutive sub-iterations satisfies the following criterion:

$$\max \left(\frac{\|\mathbf{u}_{k+1} - \mathbf{u}_k\|_\infty}{\max(1, \|\mathbf{u}_k\|_\infty)}, \frac{\|p_{k+1} - p_k\|_\infty}{\max(1, \|p_k\|_\infty)} \right) \leq 10^{-8}, \tag{1.18}$$

which is small enough to guarantee the independence of the global solution and is easily obtained after a few sub-iterations.

The transport equation of the conformation tensor (1.11) is solved using a Strang operator splitting combined, for accuracy, with a log transform of the hyperbolic transport equation

$$\left. \begin{aligned} & \text{Advection I – Solve for } \mathbf{c}^{n+(1/3)} : \\ & \frac{1}{dt/2} \left(\log \mathbf{c}^{n+(1/3)} - \log \mathbf{c}^n \right) + \left(\mathbf{u}^{n+1} \cdot \nabla \right) \log \mathbf{c}^{n+(1/3)} = 0. \\ & \text{ODE – Set } \mathbf{c}(t_n) = \mathbf{c}^{n+(1/3)} \text{ and solve for } \mathbf{c}^{n+(2/3)} = \mathbf{c}(t_n + dt) : \\ & \dot{\mathbf{c}} - \left(\nabla \mathbf{u}^{n+1} \right) \mathbf{c} - \mathbf{c} \left(\nabla \mathbf{u}^{n+1} \right)^\top + \frac{1}{Wi} \left(g(\mathbf{c}) \mathbf{c} - h(\mathbf{c}) \mathbf{I}_d \right) = 0. \\ & \text{Advection II – Solve for } \mathbf{c}^{n+1} : \\ & \frac{1}{dt/2} \left(\log \mathbf{c}^{n+1} - \log \mathbf{c}^{n+(2/3)} \right) + \left(\mathbf{u}^{n+1} \cdot \nabla \right) \log \mathbf{c}^{n+1} = 0, \end{aligned} \right\} \tag{1.19}$$

with dt the time step and *ODE* the ordinary differential equation. In practice, dt is adaptive and monitored in the interval $[10^{-6}, 10^{-3}]$ in order to reduce the total computation time,

while always satisfying the following criterion:

$$\max \left(\frac{\|\mathbf{u}^{n+1} - \mathbf{u}^n\|_\infty}{\max(1, \|\mathbf{u}^n\|_\infty)}, \frac{\|p^{n+1} - p^n\|_\infty}{\max(1, \|p^n\|_\infty)}, \frac{\|\mathbf{c}^{n+1} - \mathbf{c}^n\|_\infty}{\max(1, \|\mathbf{c}^n\|_\infty)} \right) \leq 10^{-4}. \quad (1.20)$$

For each cell, the local ordinary differential equation corresponding to the relaxation is solved using a first-order implicit Euler scheme with local sub-cycling

$$\frac{1}{\delta t} (\mathbf{c}_{k+1} - \mathbf{c}_k) = \nabla \mathbf{u}^{n+1} \mathbf{c}_{k+1} + \mathbf{c}_{k+1} \left(\nabla \mathbf{u}^{n+1} \right)^\top - \frac{1}{Wi} (g(\mathbf{c}_{k+1}) \mathbf{c}_{k+1} - h(\mathbf{c}_{k+1}) \mathbf{I}_d), \quad (1.21)$$

where δt is a local time step on each mesh element which is set to $\delta t = dt/a$, with a the smallest integer number such that $\delta t \leq 1/(100\|\nabla \mathbf{u}^{n+1}\|_\infty)$, to preserve the positive definiteness of the conformation tensor; see Mokhtari *et al.* (2023).

The solver is implemented as a specific module of CALIF³S (CALIF3S 2021). Calculations were performed on TotalEnergies' supercomputer Pangea II. Parallel computations were carried out using a domain decomposition approach based on the METIS (4.0.3) graph partitioner (Karypis & Kumar 1998) and the library OpenMPI (3.1.5) (Graham, Woodall & Squyres 2005). As an example to illustrate the cost of the calculations, one point in the stationary case required approximately 10^3 cores \times hours while the case ($\beta = 10$, $Wi = 84$) alone required approximately 10^5 cores \times hours.

1.5. Time averaging and root mean square variations

The time-averaged value of a variable φ over the interval $[t_1, t_2]$ is defined as

$$\bar{\varphi} = \frac{1}{t_2 - t_1} \int_{t_1}^{t_2} \varphi(\tau) \, d\tau, \quad (1.22)$$

and the corresponding root mean square (r.m.s.) is defined as

$$\varphi_{rms} = \sqrt{(\varphi - \bar{\varphi})^2}. \quad (1.23)$$

1.6. Kymographs

For the kymographs, the variable ψ is averaged along the vertical direction using the operator $\langle \psi \rangle^y = (1/L_y) \int_0^{L_y} \psi(x, y) \, dy$, where L_y corresponds to the domain height. The spatial average is then normalized by the time average as $(\langle \psi \rangle^y - \langle \bar{\psi} \rangle^y) / \langle \bar{\psi} \rangle^y$. Kymographs display this field – averaged in the y direction – along the horizontal direction over time.

1.7. Power spectral density

The power spectral density $S(f)$ of a signal φ discrete in time is given by

$$S(f) = \sum_{k=1}^K A(k) \exp(-2\pi i f k), \quad (1.24)$$

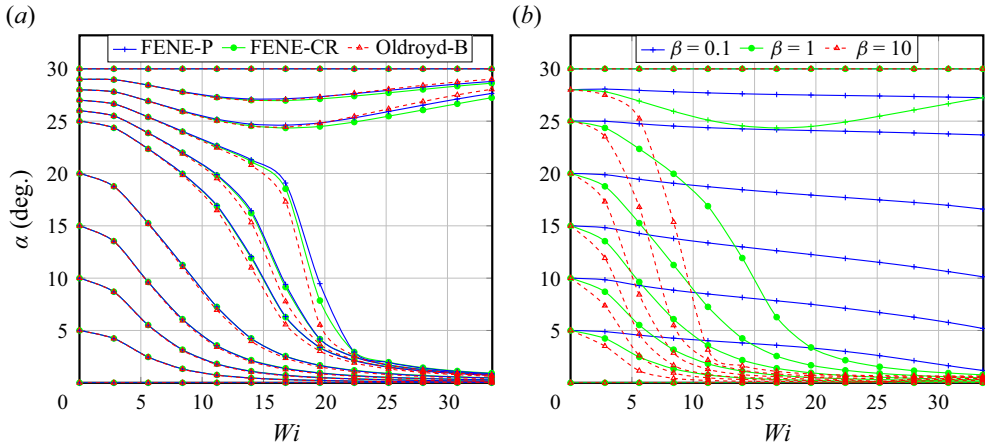


Figure 2. Steady viscoelastic flow through a hexagonal lattice. (a) Plots of the angle α between the direction of the average flow velocity and x as a function of the Weissenberg number, Wi , for the viscosity ratio $\beta = 1$, different values of θ and the FENE-P, FENE-CR and Oldroyd-B models. Each curve is obtained by fixing the angle θ and progressively increasing Wi , starting from $Wi = 0$. At $Wi = 0$, the flow is Newtonian so that the average flow velocity is along the direction of the forcing term and the value of θ for each curve can be determined as $\theta = \alpha(Wi = 0)$. (b) Plots of the angle α as a function of Wi for the Oldroyd-B model and different values of θ and β . In (a,b) points are actual computations and lines are just guides for the eyes; graphs are limited to the range $\theta \in [0, 30^\circ]$ because of the 6-fold rotational symmetry combined with the reflection symmetry about the x axis; and the Weissenberg number is defined with a reference velocity different from the averaged flow velocity, so that Wi values may seem larger than in other studies. For comparison purposes, the same figure is provided in figure 3 of the supplementary material for a Weissenberg number defined with the average flow velocity.

with K the number of discrete values. This corresponds to the discrete Fourier transform of the auto-correlation function $A(k)$ defined by

$$A(k) = \frac{1}{K} \sum_{n=1}^K \varphi(n)\varphi(n - k). \tag{1.25}$$

2. Results

2.1. Steady base flows

Our first objective is to study how steady-state strands generated in the wake of an obstacle (Haward *et al.* 2018) interact with other obstacles to guide the flow through the lattice. Since strands direct the flow through the porous structures (Mokhtari *et al.* 2022) and thus define the orientation of the flow, our main observable is the angle α between the average velocity field (\mathbf{u}) and the x axis, which is a proxy for the orientation of the strands. Our idea is to study how the system responds to changes in the forcing term, first starting in figure 2(a) with variations of the Weissenberg number Wi for fixed values of the angle θ of the force density \mathbf{f} (as defined in figure 1). In our simulations, we proceeded by progressively increasing the Weissenberg number, starting from $Wi = 0$, for each value of θ . The case $Wi = 0$ is Newtonian, so that the observed flow angle is the same as the angle of the imposed force density, $\theta = \alpha(Wi = 0)$. Upon increasing Wi , results in figure 2(a) indicate the clear formation of two preferential flow directions at $\alpha = 0^\circ$ and $\alpha = 30^\circ$ for three different constitutive relations (Oldroyd-B, FENE-P and

A web of sticky strands

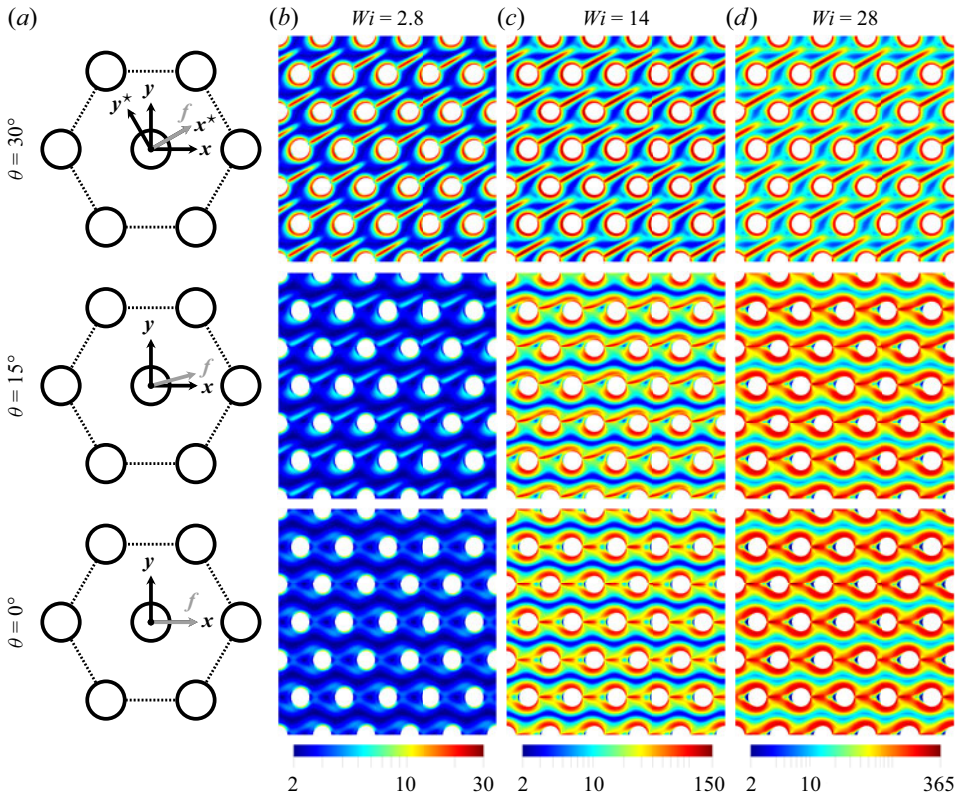


Figure 3. Steady viscoelastic flow through a hexagonal lattice of cylindrical obstacles. Fields of polymer stretching – the trace of the conformation tensor, $\text{tr}(\mathbf{c})$ – for the Oldroyd-B model with a ratio of polymer to solvent viscosities $\beta = 1$ and different values of the Weissenberg number Wi and angles θ from the aligned configuration.

FENE-CR). **Figure 3** shows that the preferential directions correspond to strands that stick to other obstacles (e.g. for $\theta = 15^\circ$), either to the closest neighbours at 0° and 60° or to the second closest at 30° . The fact that three models describing slightly different physics all yield similar results demonstrates robustness across constitutive laws. An example corresponding to the case $\theta = 25^\circ$ is given in supplementary movie 1 for the Oldroyd-B model.

We hypothesized that the mechanism that makes strands appear sticky is a feedback between the transport of the conformation tensor and the flow, which is reminiscent of the amplification mechanism of preferential flow paths in the case of side-by-side obstacles (Hopkins *et al.* 2021) (see also Mokhtari *et al.* 2022). To illustrate this effect, let us consider again the case $\theta = 25^\circ$ in supplementary movie 1. Initially, strands tend to form an angle of 25° in the wake of each circle, such that the distance with the circle immediately below is smaller than the distance with the circle above. The flow path of least resistance is above the strands with a positive feedback loop that tends to curve the streamlines towards the path of lowest flow rate and thus displace the strands further down, until eventually the path below is completely closed.

To test this hypothesis, we studied the behaviour of the strands for different values of the parameter β . As detailed in Mokhtari *et al.* (2022), β modulates the feedback of the strands upon the flow field – it is a prefactor of the divergence of the conformation tensor and thus

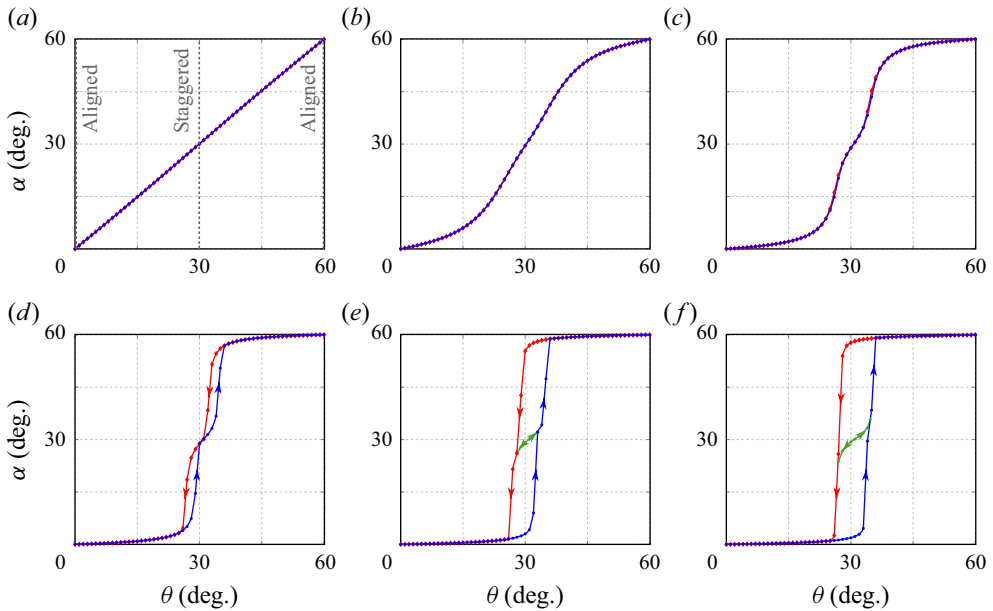


Figure 4. Bifurcation diagrams with the angle θ of the force density showing multistability and hysteresis for the Oldroyd-B model with $\beta = 1$. In blue, we present the results obtained when increasing θ from 0 to 60° and in red those obtained when decreasing θ from 60° to 0 . To obtain the green curves, we proceeded by either using the results from a point $\alpha \simeq 45^\circ$ on the blue curve as the initial condition and progressively decreasing θ , or from a point $\alpha \simeq 15^\circ$ on the red curve and increasing θ . Points are actual computations and lines are just guides for the eyes: (a) $Wi = 1.4$; (b) $Wi = 8.4$; (c) $Wi = 14.0$; (d) $Wi = 19.6$; (e) $Wi = 25.2$; and (f) $Wi = 28.0$.

acts as a weight for the polymer-associated force in the momentum transport equation. For instance, the limit $\beta \rightarrow 0$, which may be thought of as the limit of vanishingly small polymer concentration, eliminates completely the feedback of the polymers upon the flow with a velocity field given by Stokes flow and the conformation tensor by (1.11) with a fixed Stokes velocity. The graph in figure 2(b) shows that, for $\beta = 0.1$, the preferential flow directions almost completely disappear and strands do not stick to other obstacles. When $\beta = 10$, however, strands are sticky for even smaller Weissenberg numbers, thus suggesting that stickiness does indeed result from a feedback between the transport of the conformation tensor and flow.

To further understand the sticky properties of the strands, we next study the variations of the flow angle α with the force angle θ for fixed values of Wi . Figure 4 shows in blue how α evolves when progressively increasing θ from 0 to 60° . In the limit of small Weissenberg numbers, we observe a linear behaviour that is characteristic of the Newtonian case. For a moderate value of the Weissenberg number ($Wi = 8.4$), the evolution of the blue curve resembles a sigmoid, which is a signature of strands interacting with the closest obstacles (distance S at 0° and 60°). For $Wi = 14$, the shape of the blue curve changes for $\theta \simeq 30^\circ$ with strands that are long enough to reach the second closest obstacle (distance $\sqrt{3}S$ at 30° in the staggered direction), thus creating a preferential flow direction at $\alpha \simeq 30^\circ$ and breaking the linearity of the blue curve in the corresponding neighbourhood. This effect evolves non-monotonically with the Weissenberg number, with only a small perturbation in the blue curve for $Wi = 8.4$, a clear preferential direction at $Wi = 14$ and $Wi = 19.6$ and a complete disappearance of this effect for $Wi = 28$. For the largest Wi values, this is

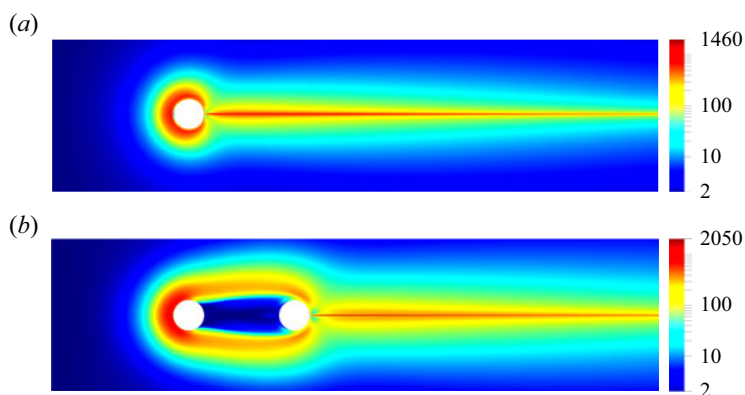


Figure 5. Illustration of the concept of the envelope. (a) Strand in the wake of a single cylinder (b) envelope of stress wrapping two cylinders aligned with the flow ($\beta = 1$, $Wi = 200$ and the distance between the centres of the two cylinders is equal to seven times the radius of the cylinders). Colours indicate the value of $\text{tr}(\mathbf{c})$. The boundary conditions are left–right and top–bottom periodicity with a channel of sufficient length to avoid boundary effects – only a small part of this channel is shown here. The characteristic distance is the channel height $H = 20$. Details of these calculations and a more thorough discussion of this problem can be found in Mokhtari *et al.* (2022).

because the interactions of the horizontal strands with the closest obstacles at $\alpha \simeq 0^\circ$ get stronger, so that ultimately detachment from the horizontal position occurs for $\theta > 30^\circ$ and the strands switch directly from $\alpha = 0^\circ$ to $\alpha = 60^\circ$. At obstacle scale, this increase in the strength of the interaction and in the stability of the flow at $\alpha \simeq 0^\circ$ corresponds to a doubling of the strand with the formation of an envelope of stress wrapped around the obstacles – a minimal example showing that these envelopes result from the interaction of strands with downstream obstacles is provided in figure 5 and additional details can be found in Mokhtari *et al.* (2022).

This threshold effect in θ with strands strongly sticking to closest neighbours is associated with subcritical bifurcations and hysteresis. Figure 4 also shows in red the path obtained when decreasing θ starting from $\theta = 60^\circ$. Symmetrically, the strands are now stuck to the closest neighbours at 60° and the transition occurs for lower values of θ compared with the blue curve. We can also recover an intermediate path at 30° – in green in figure 4 – by either decreasing θ starting from an initial condition corresponding to a point at $\alpha \simeq 45^\circ$ on the blue curve or increasing θ from a point at $\alpha \simeq 15^\circ$ on the red curve. This green path corresponds to strands sticking to the second closest neighbours but can only be obtained when the strands are not initially stuck to the closest neighbours. We further observe two hysteresis regimes with the Weissenberg number. For $Wi = 19.6$, there are two separate hysteretic loops featuring bistability around $\alpha = 0^\circ$ and 30° or around $\alpha = 30^\circ$ and 60° . These loops then meet to yield tristability around $\alpha = 0^\circ$, 30° and 60° (see example for $Wi = 24$ in supplementary movie 2 for the Oldroyd-B model). The (θ, Wi) phase diagram in figure 6 summarizes the different regimes and shows insets of the corresponding stretching field.

2.2. Destabilization and unsteady flows

Upon further increasing the Weissenberg number, we observe a spontaneous transition to unsteady flows with strands that initially form along the direction of the force and then destabilize. To study this transition, we focus on the FENE-CR model to avoid

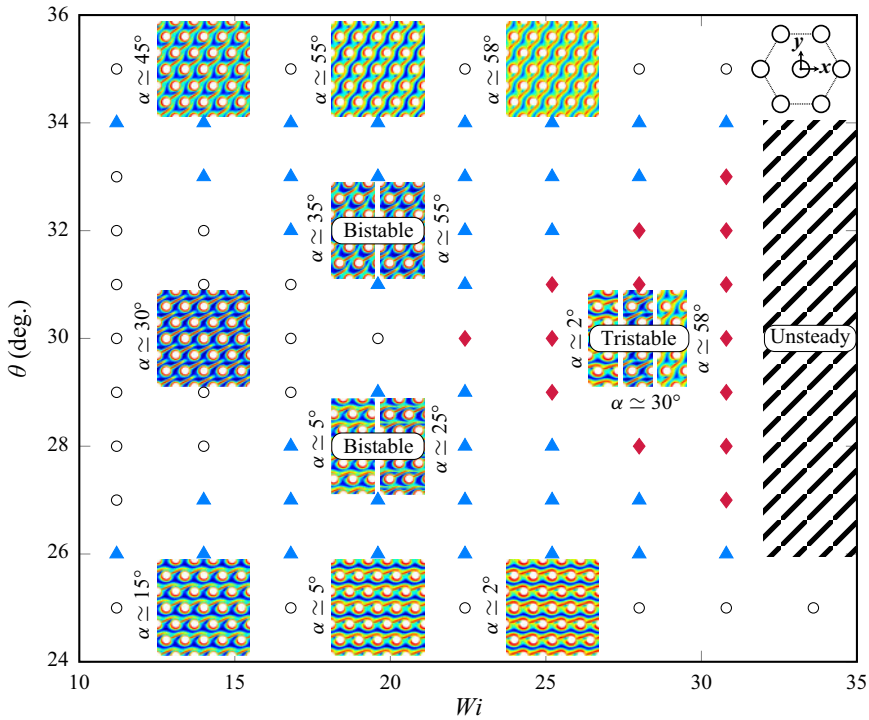


Figure 6. The (θ, Wi) phase diagram with the different stability domains for the Oldroyd-B model with $\beta = 1$. Insets show the corresponding polymer stretching fields and the position of the strands; (○) indicates a single stable state, (▲, blue) bistability and (◆, red) tristability. Stripes indicate a transition towards unsteady flows.

complications associated with shear thinning (vs FENE-P) (Herrchen & Öttinger 1997) and to maximize accuracy (vs Oldroyd-B) (Kim *et al.* 2005; Mokhtari *et al.* 2023). Since multistability occurs for the staggered direction $\theta = 30^\circ$, we expect the most interesting dynamics to develop for this case and therefore consider it first – as we will see, the multistability previously described in the steady state is important to understand the dynamics. We proceed by placing ourselves in the frame of reference (x^*, y^*) (see definition in figure 1), rather than changing the angle of the forcing term in the aligned direction $\theta = 0^\circ$. Since we use a structured mesh, this approach makes it easier to match the symmetries of the mesh with that of the problem – closest neighbours are at -30° and $+30^\circ$ angles in (x^*, y^*) , rather than 0° and 60° in (x, y) .

Based upon our simulations, we propose a classification of the different regimes as

- (I) Self-sustained flapping oscillations about base flow.
- (II) Travelling waves with fronts separating zones with different configurations of the strands.
- (III) An intermediate regime with remaining flapping oscillations combined with large amplitude/low frequency fluctuations.
- (IV) A quasi-steady regime with no oscillations and large amplitude/low frequency fluctuations leading to a steady state.
- (V) Strands pulsations and fluctuations over a range of frequencies.

Regime (I) appears for relatively low values of β and Wi , at the onset of the transition to unsteady flow. Oscillations develop about the direction of the force density with what

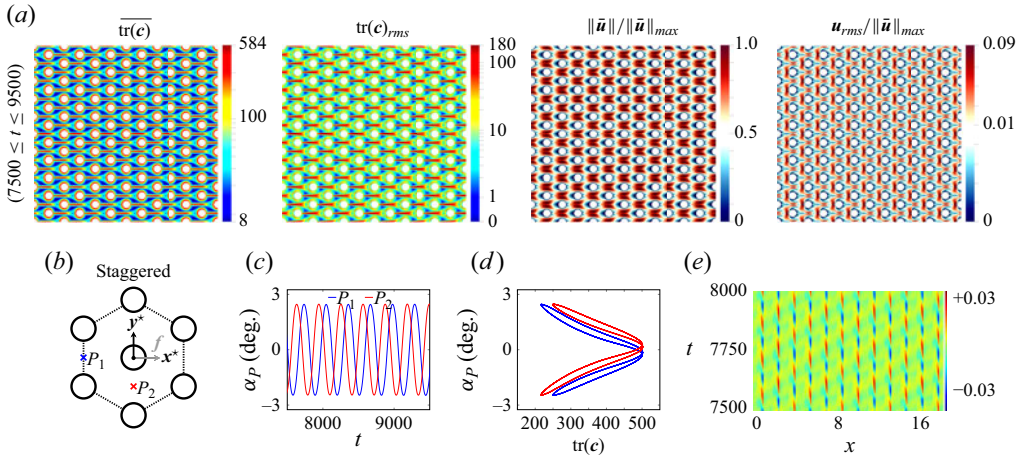


Figure 7. Regime (I): self-sustained flapping oscillations, obtained for the FENE-CR model with $b = 1000$ and $(\beta = 0.5, Wi = 47.6)$. (a) The first and second columns show the time-averaged field of the trace of the conformation tensor and the corresponding r.m.s. variations, respectively, for the time interval $(7500 \leq t \leq 9500)$. The third and fourth columns show the normalized time-averaged field of the velocity and the corresponding r.m.s. variations, respectively. (b) Definition of the points of interest P_1 (blue) and P_2 (red) in the staggered configuration. Here, f shows the direction of the volume force. (c) Time variations of the local velocity angle α_P at P_1 and P_2 . (d) Phase diagrams with α_P as a function of the local trace of the conformation tensor at P_1 and P_2 . (e) Kymographs of $\overline{\text{tr}(c)}$ averaged over the vertical direction and normalized by its time average.

appears to be a Hopf bifurcation (see supplementary movie 3). Figure 7(a) shows that the average position of the strands, as visible on the field of the time average of the trace of the conformation tensor, $\overline{\text{tr}(c)}$, is horizontal with r.m.s. variations about this position. The time-averaged flow in the wake of each cylinder is similar to the steady case, with strands essentially acting as a tangential force opposed to the flow (Mokhtari *et al.* 2022). Figures 7(b)–7(e) further show out-of-phase flapping oscillations from one row to the next.

In regime (II), strands are still relatively short but start interacting more strongly with closest neighbours at $\pm 30^\circ$. Time-averaged fields for the trace of the conformation tensor, $\overline{\text{tr}(c)}$, in figure 8(a) now show that strands tend to stick to closest neighbours and periodically switch positions. Orbits in figure 8(c,d) confirm that strands do not oscillate about the base flow configuration but rather that they stick to one side or the other, while generating a travelling wave solution in the direction of the flow (kymograph in figure 8(e) and supplementary movie 4). To understand this phenomenon, consider that each strand may be roughly thought of as a barrier allowing or preventing flow through a given pore throat. These barriers have a limited number of accessible positions. They are either stuck to one or the other neighbour and, in so doing, allow or prevent flow. Globally, strands also arrange in a way that maintains flow through the structure, this leading to a set of possible configurations. Figure 8(f) presents such solutions with strands successively sticking up and down so as to form tortuous ‘zigzag’ channels in the x direction. Figure 8(f) further shows that two topologically equivalent configurations are possible for the same type of zigzag channels. Some of the observed travelling wave solutions consist of vertically invariant zones of one of these two configurations separated by a front where strands switch side (figure 8(g) and supplementary movie 4).

In regimes (III), (IV) and (V), strands get longer and interact more strongly with other obstacles, so that initial flapping oscillations tend to disappear. We observe a stabilization

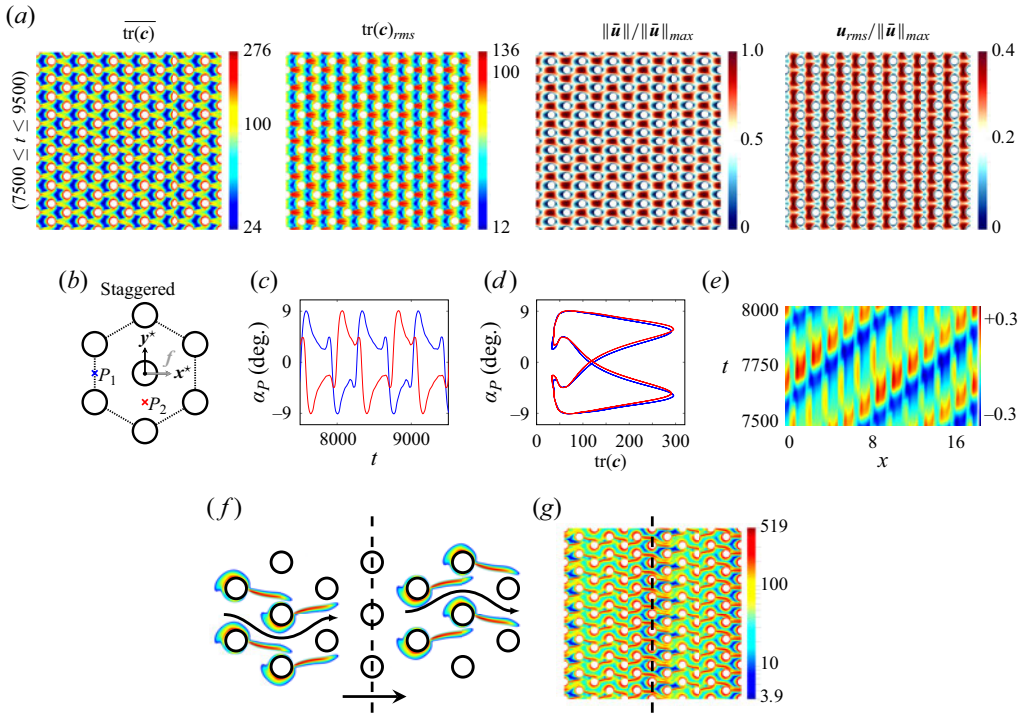


Figure 8. Regime (II): travelling waves for the FENE-CR model with $b = 1000$ and $(\beta = 2, Wi = 47.6)$. (a) The first and second columns show the time-averaged field of the trace of the conformation tensor and the corresponding r.m.s. variations, respectively, for the time interval $(7500 \leq t \leq 9500)$. The third and fourth columns show the normalized time-averaged field of the velocity and the corresponding r.m.s. variations, respectively. (b) Definition of the points of interest P_1 (blue) and P_2 (red) in the staggered configuration. Here, f shows the direction of the volume force. (c) Time variations of the local velocity angle α_P at P_1 and P_2 . (d) Phase diagrams with α_P as a function of the local trace of the conformation tensor at P_1 and P_2 . (e) Kymographs of $\text{tr}(c)$ averaged over the vertical direction and normalized by its time average. (f) Illustration of the two equivalent strand configurations with a travelling front (dashed line) corresponding to strands switching side. (g) Results of the simulations for $\text{tr}(c)$ for the case $(\beta = 2, Wi = 47.6)$ showing the position of the front along with the dashed line in (f).

of the zigzag channels (figure 9b,e) and, for regimes (IV) and (V), the appearance of envelopes of localized stress along the $\pm 30^\circ$ angle, whereby the cylinders are encased between two strands of high polymeric stress instead of each one generating a strand in their wake. An example from regime (IV) in figure 9(c,f) for the case $(\beta = 5, Wi = 19.6)$ shows a steady-state mix of zigzag channels and envelopes. Figure 10 shows that envelopes tend to be more prominent as we increase Wi and β in regime (V), ranging from only a few instances for $(\beta = 5, Wi = 42)$ to covering the entire lattice for $(\beta = 10, Wi = 58.8)$ with a pattern of time-averaged localized stress that is similar to that of the aligned case at steady state in figure 3. Contrary to the aligned case, however, this pattern now implies that there is a misalignment between the flow and the imposed force, with strands directing the flow in the $(\pm 30^\circ)$ directions, as visible from the velocity fields in figure 10. We hypothesized that this phenomenon is the consequence of the stability of the envelope pattern at $\pm 30^\circ$. To test this hypothesis, we performed calculations in the aligned case and show in figure 4 of the supplementary material that this pattern is associated with a much simpler dynamics, where envelopes remain stable over a wide range of values of β and Wi .

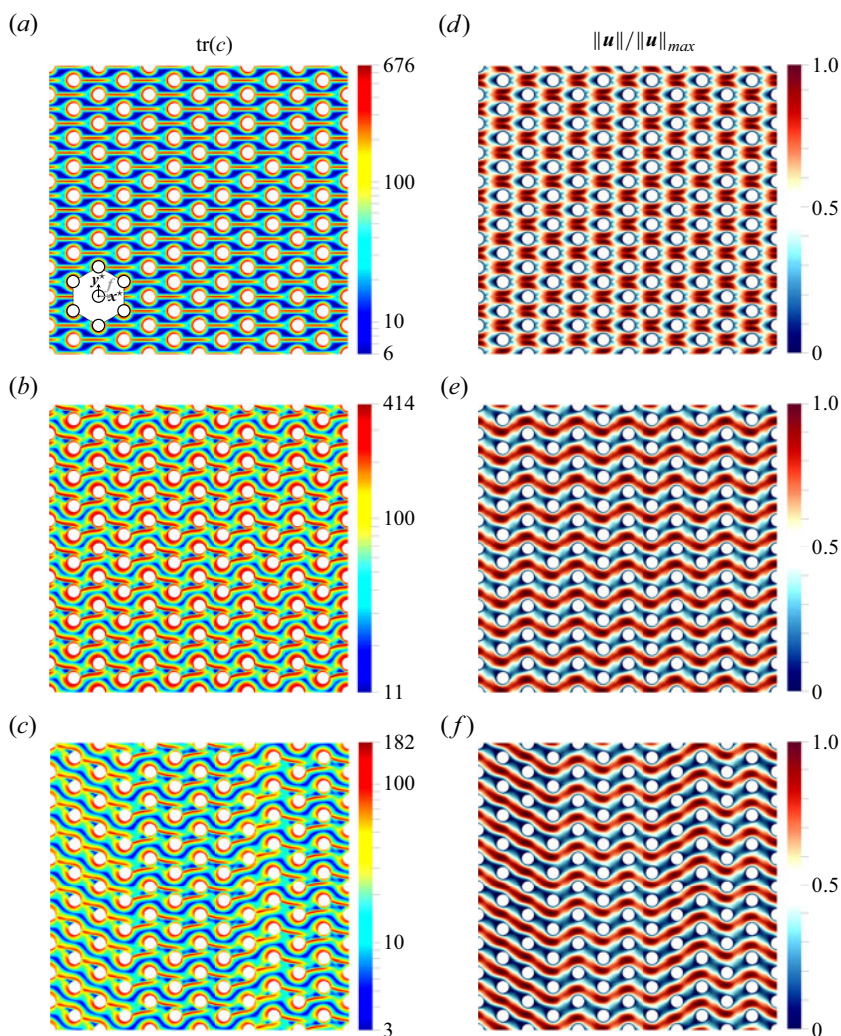


Figure 9. Examples of steady-state fields for $\text{tr}(c)$ and the corresponding normalized amplitude of the velocity; (a) ($\beta = 0.5$, $Wi = 42$) corresponds to the trivial steady solution, (b) ($\beta = 1$, $Wi = 53.2$) to the regime (III) and (c) ($\beta = 5$, $Wi = 19.6$) to regime (IV).

In these regimes, we also observe defects at the junction of zones with different stress configurations, for example between envelopes and zigzags as visible on the top right of figure 10(b) for $\text{tr}(c)$. These defects are sometimes displaced through the lattice of obstacles, as shown in figure 10(a), or are stable in a given position, as shown in figure 10(b). The propagation of a defect through the structure occurs in a variety of ways, ranging from slow propagation from neighbour to neighbour to large puffs of rapid strand movements, as illustrated in figure 10(a). In many instances, the defects are only ephemeral and ultimately disappear (supplementary movie 6a and b), leading to a stable pattern of strands. In regime (V), we observe beatings/pulsations that develop along the strands (supplementary movies 5 and 6a and b) with a stable pattern of stress and no change in the network of flow channels. Examples of such pulsations are presented in fields of $\text{tr}(c)_{rms}$ in figure 10 at both $\beta = 5$ and $\beta = 10$.

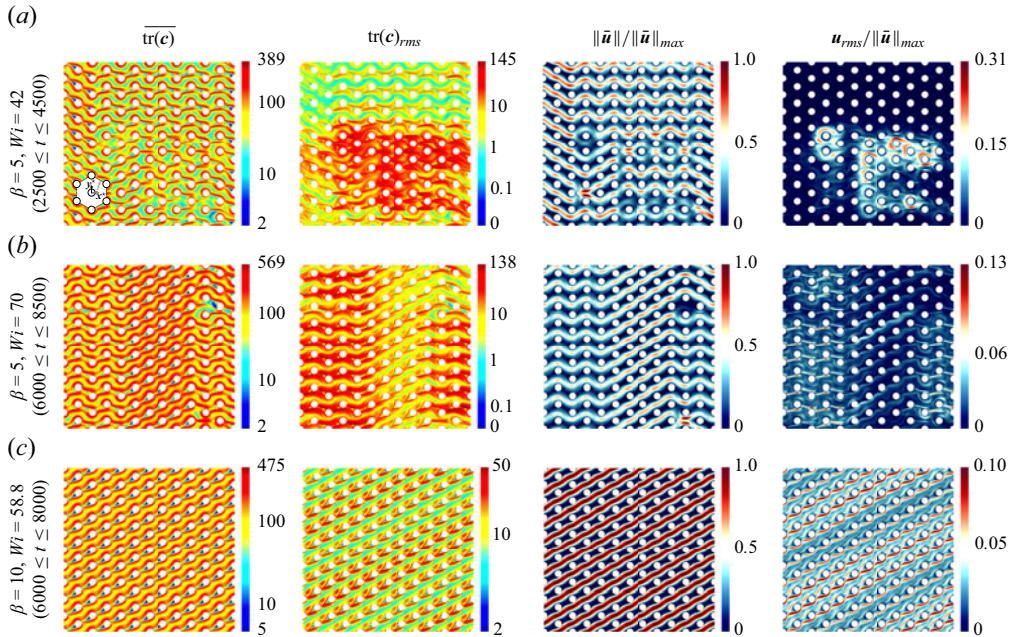


Figure 10. Regime (V): strand pulsations for the FENE-CR model with $b = 1000$. Each line corresponds to a set of dimensionless numbers with results presented for different time intervals. The first and second columns show the time-averaged fields of the trace of the conformation tensor and the corresponding r.m.s. variations, respectively. The third and fourth columns show the normalized time-averaged fields of the velocity and the corresponding r.m.s. variations, respectively.

Figure 11 summarizes the different regimes in a (Wi, β) diagram and illustrates the corresponding variations in time of the global flow angle α . Regime (I) at $(\beta = 0.5, Wi = 47.6)$ features distinct oscillations of α that correspond to the periodic flapping motion of the birefringent strands – the power spectrum has a clear dominant frequency (see figure 12). In regime (II), we also have clear oscillations with strands that successively stick to closest neighbours and a distinct frequency in the power spectrum (see figure 12). For regimes (III), (IV) and (V), strands stick strongly to obstacles and the initial flapping oscillations tend to disappear, with few remaining oscillations in regime (III) (figure 11) and only low frequency/large amplitude temporal fluctuations in regimes (IV) and (V) (figure 11). For regime (V), we observe pulsations at later times that are very different in nature from the self-sustained oscillations in regime (I). They feature a more complex temporal response and a power spectrum (see figure 12) that has no distinct frequency, but rather shows some of the hallmarks of chaos and elastic turbulence (Groisman & Steinberg 2000; Steinberg 2021). Calculations in the aligned case, as presented in the supplementary material figure 4, also show pulsations with a similar spectral response (see figure 12). This regime is the only unsteady bifurcation that we were able to observe in the aligned case, thus suggesting that strand beating pulsations are integral to the transition towards elastic turbulence.

3. Discussion

Our simulations do not represent a perfect description of experiments, such as those performed in Walkama *et al.* (2020) or Haward *et al.* (2021b). Due to computational

A web of sticky strands

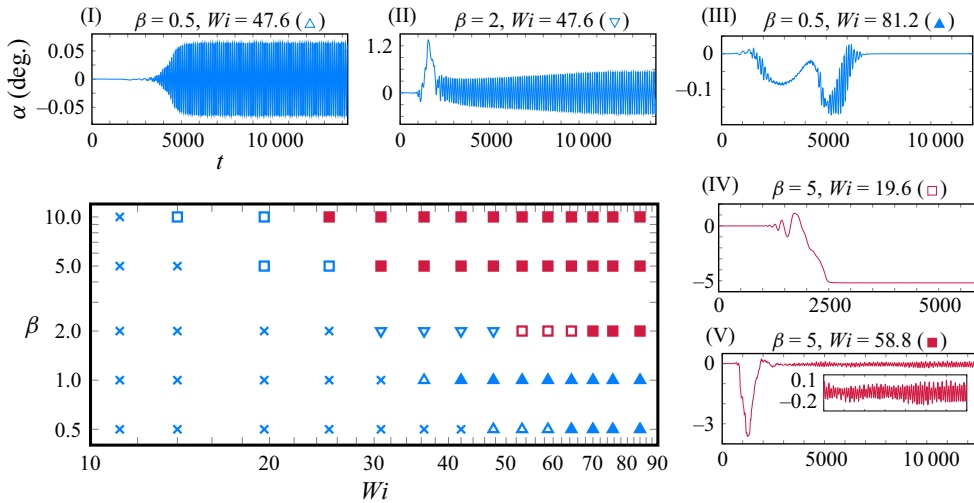


Figure 11. Diagram of the different regimes obtained for the FENE-CR with $b = 1000$ in the staggered configuration. The main graph shows the different regimes as a function of β and Wi . The other plots are examples of time evolutions of α for each regime. The colour code indicates whether the strands remain short (blue), without envelope formation or become long and form envelopes (red). Here, (\times , blue) corresponds to the trivial steady solution (figure 9(a,d)), (Δ , blue) to oscillations in regime (I), (∇ , blue) to travelling fronts in regime (II), (\blacktriangle , blue) to the intermediate in regime (III), (\square , red) to the quasi-steady regime (IV) and (\blacksquare , red) to the pulsations in regime (V).

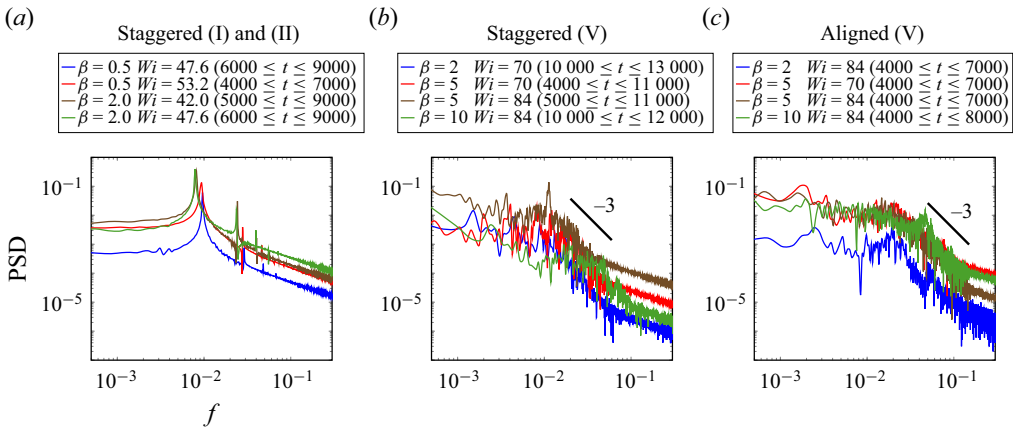


Figure 12. Power spectral density associated with the temporal fluctuation of α for different values of the parameters β and Wi . The figure on the left-hand side corresponds to regimes (I) and (II) in the staggered configuration, the one at the centre to regime (V) in the staggered configuration and the one on the right-hand side to regime (V) in the aligned configuration. The dimensionless frequency f corresponds to the non-dimensionalization presented in the article (Methods). We also show the same figure in the supplementary material figure 6 for a frequency corresponding to time non-dimensionalized with the characteristic time for polymer relaxation.

limitations, we have considered a 2-D geometry based on a relatively small representative portion of the porous medium and may have thus neglected important 3-D effects. Further, we have used periodic conditions with a constant forcing term, whereas unstable flow may generate spatio-temporal variations of the locally averaged pressure gradient in real large

pore structures. Oldroyd and FENE models are also imperfect; for instance, by assuming some form of uniformity of the concentration of polymers in the porous medium. The question that we ask in this discussion section is whether, despite these limitations, we can extract useful information from our simulations to understand viscoelastic instability mechanisms in porous media. To this end, we first discuss links between our simulations and experimental results from the literature.

Sequences of transitions from self-sustained oscillations to aperiodic fluctuations have been observed in different systems involving viscoelastic fluids, such as axisymmetric contractions (McKinley *et al.* 1991) and microfluidic cylinders (Haward *et al.* 2019). Hopf bifurcations have also been found to be linked to birefringent strands in cross-slot flows (Xi & Graham 2009). Recent experiments have specifically studied the dynamics of viscoelastic flows through a staggered hexagonal lattice and point towards an excellent agreement with our simulations:

- (i) Self-sustained oscillations are evident in supplementary movie S1 in Haward *et al.* (2021b), clearly showing strands flapping from one side to the other in a way that is directly comparable to our simulations in supplementary movie 3. Similarly, the retardation field in figure 3 in Haward *et al.* (2021b) for the lowest Weissenberg numbers shares similarities with $\overline{\text{tr}(c)}$ and $\text{tr}(c)_{rms}$ in figures 7–8.
- (ii) A transition from short oscillating strands to zigzag channels is visible in figure 12D in Datta *et al.* (2022), when increasing the Weissenberg number in the staggered configuration. Supplementary movie S1 in Haward *et al.* (2021b) also shows the temporary formation of structures that are similar to our zigzag channels.
- (iii) Supplementary movies S2 and S3 in Walkama *et al.* (2020) show travelling waves with fronts that delineate zones with different strand configurations.
- (iv) Figure 3 and supplementary movie S3 in Haward *et al.* (2021b) show two strands per cylinder in the aligned case and the formation of an envelope of polymer stress.
- (v) Supplementary movies S2 and S4 in Haward *et al.* (2021b) show stable patterns of retardation that seem to exhibit some of the pulsations observed in our simulations (supplementary movie 5).

de Blois, Haward & Shen (2023) and Ström, Beech & Tegenfeldt (2023) have also demonstrated the existence of waves in polymer flows through a square lattice of obstacles. de Blois *et al.* (2023) show the emergence of elastic waves in a microfluidic canopy of either rigid or flexible slender pillars. Although the geometry and the macroscopic boundary conditions are different from our simulations, the development of large-scale coherent structures with a deflection of the flow direction could indicate that sticky birefringent strands are involved. Ström *et al.* (2023) also show waves in a microfluidic square lattice, but with important differences in the experimental approach. Ström *et al.* (2023) use DNA with a size of the polymer that is similar to that of the gap between obstacles, whereas de Blois *et al.* (2023) use hyaluronic acid with pores that are much larger than the polymers. The observed waves in Ström *et al.* (2023) correspond to polymer concentration and conformation, whereas de Blois *et al.* (2023) show waves in the velocity vector field and the deflection of flexible pillars. The geometry is also slightly different, in particular the positions of the inlet/outlets and the gap between the top of the pillars and the device cover in de Blois *et al.* (2023). Notwithstanding these technical differences, Ström *et al.* (2023) also show that there is a transition from steady depletion to cyclic fluctuations and then waves; that the waves correspond to areas of stretched polymers; that the concentration of DNA – similar to changes in β in our model – modulates the instability with no waves for sufficiently low concentrations; that there is a depletion zone

between pillars and the formation of vortices; that a slight randomization of pillar position eliminates waves. These observations suggest that the mechanisms at play could in fact be similar to that described in Walkama *et al.* (2020), Haward *et al.* (2021b), Mokhtari *et al.* (2022) and the present work. Future simulations in square lattices should clarify similarities and differences.

All of our simulations are two-dimensional. One can argue that the nature of viscoelastic instabilities arising in microfluidic systems is in essence three-dimensional. In studying the elastic instability upstream of a single cylinder – height 60 μm , diameter 50 μm and channel width 100 μm – using 3-D holographic particle velocimetry, Qin *et al.* (2019) have shown that upstream vortices initiate at the corners between the cylinder and the wall, so that these corners actually play a central role in the instability (Poole 2019). Three-dimensional flows may also develop independently from the wall effect, directly due to instabilities (Gutierrez-Castillo, Kagel & Thomases 2020). And it is difficult to think that, at very large Weissenberg numbers, fully developed elastic turbulence in porous media can remain two-dimensional, even in microfluidic systems with slender obstacles. Three-dimensional unstable simulations would therefore be extremely valuable. On the other hand, even if we could overcome the tremendous computational cost of such 3-D computations, the substantial agreement between our simulations and microfluidic experiments in Walkama *et al.* (2020) and Haward *et al.* (2021b) suggests that 2-D simulations capture some important physics. It also suggests that 2-D instabilities are a fundamental part of the problem for the slender microfluidic geometry and the transitions observed in Walkama *et al.* (2020) and Haward *et al.* (2021b).

Details in the geometry of the system and in the rheology of the fluid may further modulate the relative weight of 3-D effects and modify regimes and transitions. For instance, an obvious difference between experiments in Qin *et al.* (2019) and Haward *et al.* (2021b) is the ratio of height to diameter, which is close to 1 for Qin *et al.* (2019) and 10 in Haward *et al.* (2021b). It is possible that vortices contribute to the dynamics in both cases, but that the relative influence of the 2-D geometry and of the corners in controlling the stability strongly depends upon the ratio of height to diameter. Another difference between these experiments is that Qin *et al.* (2019) considers a single cylinder whereas Haward *et al.* (2021b) deals with an array of cylinders. The instability mechanism in the case with one cylinder involves the growth of the vortex length, which can reach several times the cylinder diameter. In inertial turbulence through porous media, the size of turbulent structures is restricted by the size of the pores (Jin *et al.* 2015). It is possible that a similar constraint exists for viscoelastic flows with upstream obstacles limiting the size of the vortex and thus the impact of the walls upon the dynamics. Ribeiro *et al.* (2014) have shown that, for the case of a single confined cylinder, shear-thinning effects have an impact on the development of elastic instabilities for a variety of aspect ratios.

What then did we learn from 2-D simulations? First, our interpretation of spatio-temporal fluctuations in terms of the stability of a web of sticky strands provides an intuitive basis for interpreting experimental results. It clarifies the link between the ‘screening’ of the stagnation points described in Haward *et al.* (2021b) and the development of instabilities. Haward *et al.* (2021b) hypothesized that stagnation points are screened from the flow in the aligned geometry – resting their argument upon example calculations of creeping flows through the different structures. They suggest that screened stagnation points lose their ‘strength’ as a source of polymer stress, inducing a delay in the occurrence of the instability. We have previously shown in Mokhtari *et al.* (2022) that this phenomenon is not only due to the geometry in Stokes flow but also stems from a feedback between flow and birefringent strands for viscoelastic flows.

When strands form an envelope around cylinders, they generate a stagnant zone between cylinders that essentially behaves like a two-sided lid-driven cavity. In the present work, we further provide a connection between the patterns of localized stress and the stability: (i) instabilities develop more easily in the absence of envelope patterns; (ii) the initial instability in the staggered case corresponds to a destabilization of individual strands in the wake of each cylinder with an initially tristable configuration at steady state and what looks like a Hopf bifurcation; (iii) the transition towards elastic turbulence corresponds to a destabilization of the envelope pattern in all our simulations – pulsations regime (V). We therefore argue that what controls the stability of the flow is the pattern of localized stress, in particular the very stable envelope pattern.

Our results also show that, in the staggered configuration, there is first a transition to unsteady flow, then a restabilization and finally a transition towards elastic turbulence. We initially observe the formation of a single strand in the wake of each cylinder, so that the first transition is likely to fit within the classical framework of viscoelastic flow past a single cylinder. The elastic instability in flows with curved streamlines is widely considered as being driven by hoop stress (Shaqfeh 1996). The Pakdel–McKinley criterion (McKinley, Pakdel & Öztekin 1996; Pakdel & McKinley 1996) quantifies this using a dimensionless parameter, M , that takes into account the relative importance of the tensile stress and the ratio of the relaxation length of a perturbation to the radius of curvature of streamlines. We thus hypothesize that the onset of the instability (regime (I)) may be treated in a way similar to § 4.2 in McKinley *et al.* (1996). The restabilization observed in regime (IV) is more puzzling. Our hypothesis is that, as the strands grow longer, they modify the stress pattern – a mixture of envelopes and zigzag channels – leading to lower values of the tensile stress and reduced curvature of the streamlines – a phenomenon that is linked to the screening of stagnation points, as discussed in Haward *et al.* (2021b). Thus, it may be possible to define a second critical value of the dimensionless number M for the onset of the regime with pulsations of the strands forming envelopes.

This picture is consistent with the non-monotonic variation of the spatially averaged retardation fluctuations with the Weissenberg number observed in Haward *et al.* (2021b). Our simulations suggest that the first increase is due to self-sustained oscillations and waves (regimes I and II), that the following decrease results from the stabilization of long strands (regimes III and IV) and that the second increase is caused by the destabilization of the envelope patterns and the appearance of strand pulsations (regime V). This is also consistent with the observation in Haward *et al.* (2021b) that the staggered and aligned configurations behave similarly at sufficiently high Weissenberg numbers: the instability in both cases corresponds to a destabilization of the envelopes. In fact, this may also suggest that the transition to elastic turbulence and chaos – not just unsteady flow – actually develops for similar Weissenberg numbers in both configurations (see figure 5 in the supplementary material), thus shining a different light on transitions in Walkama *et al.* (2020).

Another interesting observation in our simulations is what happens as we get away from transitions. We show that the problem rapidly becomes strongly nonlinear and non-local. The mechanism that drives self-sustained oscillations and waves (regimes I and II) is not only a combination of streamline curvature and large tensile stress, but also stems from interactions between the strands and obstacles and from a coupling between flow channels through the entire structure. Similarly, once pulsations develop, fluctuations in one pore modify the behaviour of neighbouring pores – an idea found in recent studies (Browne, Shih & Datta 2020a; Kumar *et al.* 2021) – emphasizing the importance of spatial

correlation, non-locality and perturbation propagation in viscoelastic flows through porous media.

4. Conclusions

At steady state, we have shown that interactions between birefringent strands and obstacles guide the flow through the 2-D structure and control the direction of the average flow. Strands tend to stick to obstacles and, in so doing, create preferential flow directions through the lattice. This phenomenon leads to a succession of subcritical bifurcations with the angle of the forcing term, which yields multistability and hysteresis. Upon further increasing the Weissenberg number Wi and the ratio of viscosities β , we discovered a rich zoology of spatio-temporal fluctuations, including self-sustained flapping oscillations, travelling wave solutions, defect propagation and strand pulsation fluctuations – this last regime being integral to the transition towards elastic turbulence. Our work demonstrates that strands and their interactions with flow and obstacles control the steady base flow, the spontaneous transition to unsteady flow and the route to chaos in 2-D lattices of obstacles. More generally, this suggests that the stability of localized stress patterns is key in understanding the transition towards elastic turbulence in complex structures.

Supplementary material and movies. Supplementary material and movies are available at <https://doi.org/10.1017/jfm.2023.916>.

Funding. The authors thank R. de Loubens, from TotalEnergies, for valuable discussions on this topic and F. Babik, from the CALIF³S development team at IRSN, for his precious support. The authors would also like to thank TotalEnergies for funding and supporting this work, in particular through access to the PANGEA II supercomputer.

Declaration of interests. The authors report no conflict of interest.

Author ORCIDs.

 Michel Quintard <https://orcid.org/0000-0002-6150-7011>;

 Yohan Davit <https://orcid.org/0000-0002-2234-9567>.

REFERENCES

- BECHERER, P., VAN SAARLOOS, W. & MOROZOV, A.N. 2009 Stress singularities and the formation of birefringent strands in stagnation flows of dilute polymer solutions. *J. Non-Newtonian Fluid Mech.* **157** (1–2), 126–132.
- BIRD, R.B., CURTISS, C.F., ARMSTRONG, R.C. & HASSAGER, O. 1987 *Dynamics of Polymeric Liquids, Volume 2: Kinetic Theory*. Wiley.
- DE BLOIS, C., HAWARD, S.J. & SHEN, A.Q. 2023 Canopy elastic turbulence: spontaneous formation of waves in beds of slender microposts. *Phys. Rev. Fluids* **8**, 023301.
- BROWNE, C.A. & DATTA, S.S. 2021 Elastic turbulence generates anomalous flow resistance in porous media. *Sci. Adv.* **7** (45), eabj2619.
- BROWNE, C.A., SHIH, A. & DATTA, S.S. 2020a Bistability in the unstable flow of polymer solutions through pore constriction arrays. *J. Fluid Mech.* **890**, A2.
- BROWNE, C.A., SHIH, A. & DATTA, S.S. 2020b Pore-scale flow characterization of polymer solutions in microfluidic porous media. *Small* **16** (9), 1903944.
- CALIF³S 2021 A computational fluid dynamics software based on Pelicans. Available at <https://gforge.irsn.fr/#/project/calif3s>.
- CLARKE, A., HOWE, A.M., MITCHELL, J., STANILAND, J. & HAWKES, L.A. 2016 How viscoelastic-polymer flooding enhances displacement efficiency. *SPE J.* **21** (03), 0675–0687.
- CLARKE, A., HOWE, A.M., MITCHELL, J., STANILAND, J., HAWKES, L. & LEEPER, K. 2015 Mechanism of anomalously increased oil displacement with aqueous viscoelastic polymer solutions. *Soft Matt.* **11** (18), 3536–3541.

- DATTA, S.S., ARDEKANI, A.M., ARRATIA, P.E., BERIS, A.N., BISCHOFBERGER, I., MCKINLEY, G.H., EGGERS, J.G., LÓPEZ-AGUILAR, J.E., FIELDING, S.M., FRISHMAN, A., *et al.* 2022 Perspectives on viscoelastic flow instabilities and elastic turbulence. *Phys. Rev. Fluids* **7** (8), 080701.
- DAUBEN, D.L. & MENZIE, D.E. 1967 Flow of polymer solutions through porous media. *J. Petrol. Tech.* **19** (08), 1065–1073.
- GALINDO-ROSALES, F.J., CAMPO-DEANO, L., PINHO, F.T., VAN BOKHORST, E., HAMERSMA, P.J., OLIVEIRA, M.S.N. & ALVES, M.A. 2012 Microfluidic systems for the analysis of viscoelastic fluid flow phenomena in porous media. *Microfluid Nanofluid* **12** (1–4), 485–498.
- GRAHAM, R.L., WOODALL, T.S. & SQUYRES, J.M. 2005 Open MPI: a flexible high performance MPI. In *International Conference on Parallel Processing and Applied Mathematics*, pp. 228–239. Springer.
- GROISMAN, A. & STEINBERG, V. 2000 Elastic turbulence in a polymer solution flow. *Nature* **405** (6782), 53–55.
- GUTIERREZ-CASTILLO, P., KAGEL, A. & THOMASES, B. 2020 Three-dimensional viscoelastic instabilities in a four-roll mill geometry at the stokes limit. *Phys. Fluids* **32** (2), 023102.
- HARLEN, O.G., RALLISON, J.M. & CHILCOTT, M.D. 1990 High-Deborah-number flows of dilute polymer solutions. *J. Non-Newtonian Fluid Mech.* **34** (3), 319–349.
- HAWARD, S.J., HOPKINS, C.C. & SHEN, A.Q. 2020 Asymmetric flow of polymer solutions around microfluidic cylinders: interaction between shear-thinning and viscoelasticity. *J. Non-Newtonian Fluid Mech.* **278**, 104250.
- HAWARD, S.J., HOPKINS, C.C. & SHEN, A.Q. 2021*b* Stagnation points control chaotic fluctuations in viscoelastic porous media flow. *Proc. Natl Acad. Sci. USA* **118** (38), e2111651118.
- HAWARD, S.J., HOPKINS, C.C., VARCHANIS, S. & SHEN, A.Q. 2021*a* Bifurcations in flows of complex fluids around microfluidic cylinders. *Lab on a Chip* **21**, 4041–4059.
- HAWARD, S.J., KITAJIMA, N., TODA-PETERS, K., TAKAHASHI, T. & SHEN, A.Q. 2019 Flow of wormlike micellar solutions around microfluidic cylinders with high aspect ratio and low blockage ratio. *Soft Matt.* **15** (9), 1927–1941.
- HAWARD, S.J., TODA-PETERS, K. & SHEN, A.Q. 2018 Steady viscoelastic flow around high-aspect-ratio, low-blockage-ratio microfluidic cylinders. *J. Non-Newtonian Fluid Mech.* **254**, 23–35.
- HERRCHEN, M. & ÖTTINGER, H.C. 1997 A detailed comparison of various FENE dumbbell models. *J. Non-Newtonian Fluid Mech.* **68** (1), 17–42.
- HOPKINS, C.C., HAWARD, S.J. & SHEN, A.Q. 2020 Microfluidics: purely elastic fluid–structure interactions in microfluidics: implications for mucociliary flows (small 9/2020). *Small* **16** (9), 2070047.
- HOPKINS, C.C., HAWARD, S.J. & SHEN, A.Q. 2021 Tristability in viscoelastic flow past side-by-side microcylinders. *Phys. Rev. Lett.* **126** (5), 054501.
- JIN, Y., UTH, M.-F., KUZNETSOV, A.V. & HERWIG, H. 2015 Numerical investigation of the possibility of macroscopic turbulence in porous media: a direct numerical simulation study. *J. Fluid Mech.* **766**, 76–103.
- KARYPIS, G. & KUMAR, V. 1998 A fast and high quality multilevel scheme for partitioning irregular graphs. *SIAM J. Sci. Comput.* **20** (1), 359–392.
- KAWALE, D., BOUWMAN, G., SACHDEV, S., ZITHA, P.L.J., KREUTZER, M.T., ROSSEN, W.R. & BOUKANY, P.E. 2017*a* Polymer conformation during flow in porous media. *Soft Matt.* **13** (46), 8745–8755.
- KAWALE, D., MARQUES, E., ZITHA, P.L.J., KREUTZER, M.T., ROSSEN, W.R. & BOUKANY, P.E. 2017*b* Elastic instabilities during the flow of hydrolyzed polyacrylamide solution in porous media: effect of pore-shape and salt. *Soft Matt.* **13** (4), 765–775.
- KHAN, M.B. & SASMAL, C. 2021 Elastic instabilities and bifurcations in flows of wormlike micellar solutions past single and two vertically aligned microcylinders: effect of blockage and gap ratios. *Phys. Fluids* **33** (3), 033109.
- KIM, J.M., KIM, C., CHUNG, C., AHN, K.H. & LEE, S.J. 2005 Negative wake generation of FENE-CR fluids in uniform and Poiseuille flows past a cylinder. *Rheol. Acta* **44** (6), 600–613.
- KUMAR, M., ARAMIDEH, S., BROWNE, C.A., DATTA, S.S. & ARDEKANI, A.M. 2021 Numerical investigation of multistability in the unstable flow of a polymer solution through porous media. *Phys. Rev. Fluids* **6**, 033304.
- KUMAR, M. & ARDEKANI, A.M. 2021 Elastic instabilities between two cylinders confined in a channel. *Phys. Fluids* **33** (7), 074107.
- MCKINLEY, G.H., PAKDEL, P. & ÖZTEKIN, A. 1996 Rheological and geometric scaling of purely elastic flow instabilities. *J. Non-Newtonian Fluid Mech.* **67**, 19–47.
- MCKINLEY, G.H., RAIFORD, W.P., BROWN, R.A. & ARMSTRONG, R.C. 1991 Nonlinear dynamics of viscoelastic flow in axisymmetric abrupt contractions. *J. Fluid Mech.* **223**, 411–456.
- MITCHELL, J., LYONS, K., HOWE, A.M. & CLARKE, A. 2016 Viscoelastic polymer flows and elastic turbulence in three-dimensional porous structures. *Soft Matt.* **12** (2), 460–468.

A web of sticky strands

- MOKHTARI, O., DAVIT, Y., LATCHÉ, J.-C. & QUINTARD, M. 2023 A staggered projection scheme for viscoelastic flows. *Math. Modelling Numer. Anal.* **57** (3), 1747–1793.
- MOKHTARI, O., LATCHÉ, J.-C., QUINTARD, M. & DAVIT, Y. 2022 Birefringent strands drive the flow of viscoelastic fluids past obstacles. *J. Fluid Mech.* **948**, A2.
- PAKDEL, P. & MCKINLEY, G.H. 1996 Elastic instability and curved streamlines. *Phys. Rev. Lett.* **77** (12), 2459.
- POOLE, R.J. 2019 Three-dimensional viscoelastic instabilities in microchannels. *J. Fluid Mech.* **870**, 1–4.
- QIN, B., SALIPANTE, P.F., HUDSON, S.D. & ARRATIA, P.E. 2019 Flow resistance and structures in viscoelastic channel flows at low Re . *Phys. Rev. Lett.* **123** (19), 194501.
- RANNACHER, R. & TUREK, S. 1992 Simple nonconforming quadrilateral stokes element. *Numer. Meth. Partial Differ. Equ.* **8**, 97–111.
- RIBEIRO, V.M., COELHO, P.M., PINHO, F.T. & ALVES, M.A. 2014 Viscoelastic fluid flow past a confined cylinder: three-dimensional effects and stability. *Chem. Engng Sci.* **111**, 364–380.
- SERIGHT, R.S., FAN, T., WAVRIK, K. & DE CARVALHO BALABAN, R. 2011 New insights into polymer rheology in porous media. *SPE J.* **16** (01), 35–42.
- SHAQFEH, E.S.G. 1996 Purely elastic instabilities in viscometric flows. *Annu. Rev. Fluid Mech.* **28** (1), 129–185.
- SHAQFEH, E.S.G. & KHOMAMI, B. 2021 The Oldroyd-B fluid in elastic instabilities, turbulence and particle suspensions. *J. Non-Newtonian Fluid Mech.* **298**, 104672.
- STEINBERG, V. 2021 Elastic turbulence: an experimental view on inertialess random flow. *Annu. Rev. Fluid Mech.* **53**, 27–58.
- STRÖM, O.E., BEECH, J.P. & TEGENFELDT, J.O. 2023 Short and long-range cyclic patterns in flows of dna solutions in microfluidic obstacle arrays. *Lab on a Chip* **23** (7), 1779–1793.
- VARSHNEY, A. & STEINBERG, V. 2017 Elastic wake instabilities in a creeping flow between two obstacles. *Phys. Rev. Fluids* **2** (5), 051301.
- VARSHNEY, A. & STEINBERG, V. 2019 Elastic alfvén waves in elastic turbulence. *Nat. Commun.* **10** (1), 1–7.
- WALKAMA, D.M., WAISBORD, N. & GUASTO, J.S. 2020 Disorder suppresses chaos in viscoelastic flows. *Phys. Rev. Lett.* **124** (16), 164501.
- XI, L. & GRAHAM, M.D. 2009 A mechanism for oscillatory instability in viscoelastic cross-slot flow. *J. Fluid Mech.* **622**, 145–165.